Colloids and Surfaces A: Physicochemical and Engineering Aspects 711 (2025) 136342

Contents lists available at ScienceDirect

Colloids and Surfaces A: Physicochemical and Engineering Aspects

journal homepage: www.elsevier.com/locate/colsurfa

Enhancement of photocatalytic activity of 2D/2D Sb_2WO_6/g-C_3N_4 Z-scheme heterojunction *via* effective interfacial charge transfer

Jinxin Liu [a], Jinyuan Liu [a,b,*], Qichang Peng [a], Bin Wang [b,**], Xingwang Zhu [c], Xue Gao [a], Huaming Li [a], Hui Xu [a,d,*], Paul K. Chu [b,**]

[a] School of the Environment and Safety Engineering, Institute for Energy Research, Jiangsu University, 301 Xuefu Road, Zhenjiang 212013, PR China
[b] Department of Physics, Department of Materials Science and Engineering, and Department of Biomedical Engineering, City University of Hong Kong, Tat Chee Avenue, Kowloon, Hong Kong, PR China
[c] Institute of Technology for Carbon Neutralization, College of Environmental Science and Engineering, Yangzhou University, Yangzhou 225009, PR China
[d] Jiangsu Collaborative Innovation Center of Technology and Material of Water Treatment, Suzhou University of Science and Technology, Suzhou 215009, PR China

HIGHLIGHTS

- 2D/2D g-C_3N_4/Sb_2WO_6 Z-scheme heterojunction are synthesized by electrostatic self-assembly.
- The Z-scheme heterojunction and interface contacts between 2D g-C_3N_4 and 2D Sb_2WO_6 accelerate charge transfer.
- The photocatalytic degradation rate of g-C_3N_4/Sb_2WO_6 is significantly improved.
- The photocatalytic mechanism of 2D/2D Z-scheme heterojunction is proposed.

GRAPHICAL ABSTRACT

Sb_2WO_6 ultra-thin nanosheets were synthesized using cetyltrimethyl ammonium bromide (CTAB) as an auxiliary agent. Sb_2WO_6/g-C_3N_4 materials with Z-scheme heterostructures were prepared by electrostatic self-assembly. The experimental results of photocatalytic degradation of RhB and MBT show that Sb_2WO_6/g-C_3N_4 photocatalyst has better degradation performance than Sb_2WO_6 and g-C_3N_4. The key role of hole (h^+), superoxide anion ($\cdot O_2^-$) and singlet oxygen ($^1O_2$) in the catalytic degradation process was demonstrated by electron spin resonance (ESR) and free radical trapping experiments. The enhanced photocatalytic activity can be attributed to the effective separation of photogenerated carriers in Z-scheme heterojunctions.

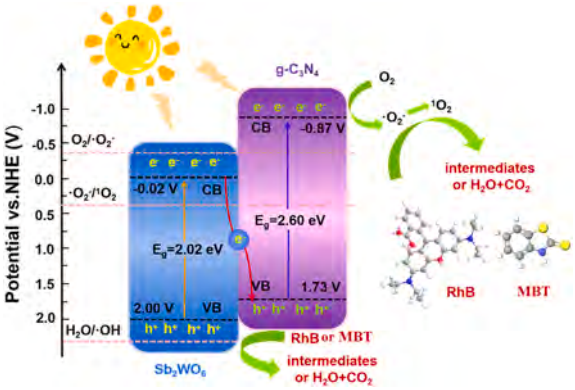

ARTICLE INFO

Keywords:
g-C_3N_4

ABSTRACT

A Z-scheme heterojunction is designed and demonstrated to enhance the separation efficiency of photocatalytic carriers. In this paper, the 2D/2D Sb_2WO_6/g-C_3N_4 (SWO/CN) Z-scheme heterojunction fabricated by electrostatic

* Corresponding authors at: School of the Environment and Safety Engineering, Institute for Energy Research, Jiangsu University, 301 Xuefu Road, Zhenjiang 212013, PR China.
** Corresponding authors.
E-mail addresses: jyliu@ujs.edu.cn (J. Liu), bwang63@cityu.edu.hk (B. Wang), xh@ujs.edu.cn (H. Xu), paul.chu@cityu.edu.hk (P.K. Chu).

https://doi.org/10.1016/j.colsurfa.2025.136342
Received 26 October 2024; Received in revised form 10 January 2025; Accepted 4 February 2025
Available online 5 February 2025

Sb_2WO_6
Z-scheme heterojunction
2D/2D
Photocatalytic degradation

self-assembly has better degradation activity than individual Sb_2WO_6 and g-C_3N_4. The rate constant K (0.0194 min^{-1}) of RhB degradation by 40 % SWO/CN was higher than that of Sb_2WO_6 (0.0054 min^{-1}) and g-C_3N_4 (0.0039 min^{-1}). The rate constant K of 40 % SWO/CN for MBT degradation was 0.4391 h^{-1}, which was 2.96 and 9.32 times that of g-C_3N_4 (0.1484 h^{-1}) and Sb_2WO_6 (0.0471 h^{-1}). The photocurrent response and electrochemical impedance spectroscopy (EIS) reveal that the Z-scheme heterojunction facilitates the separation of photogenerated charge carriers. Electron spin resonance (ESR) and radical trapping experiments demonstrate the pivotal roles of holes (h^+), superoxide ($\cdot O_2^-$), and singlet oxygen ($^1O_2$) in the catalytic degradation process. The results provide insights into the design of high-performance 2D/2D Z-scheme photocatalysts and a fundamental framework for further enhancement.

1. Introduction

Nowadays, photocatalytic technology is widely studied in the field of environmental governance and renewable energy [1–3]. The research on the treatment of organic pollutants in water environment by photocatalytic technology has great prospects [4,5]. However, there are some key problems with photocatalytic technology, such as how to improve the efficiency of photogenerated carrier separation [6–8]. Therefore, it is urgent to develop a photocatalyst that can efficiently separate photogenerated carriers. Since the discovery of single-layer graphene, photocatalysts based on two-dimensional (2D) materials have become attractive in photocatalytic applications [9,10]. Ultra-thin two-dimensional structures with large surface areas accelerate electron-hole separation. Graphitized carbon nitride (g-C_3N_4), as a metal-free polymer semiconductor material, has attracted much attention due to its advantages such as moderate energy gap (2.7 eV), good chemical stability, large specific surface area and non-toxicity [11,12]. However, the high photogenerated carrier recombination rate of g-C_3N_4 seriously restricts its application [13]. The photocatalytic activity was improved by morphological modification, defect engineering, doping and heterostructure construction [14]. Among them, the Z-scheme heterojunction boasting a large reductive oxidation capacity is suitable for the generation of holes and free radicals [15].

The layered Sb_2WO_6 is an Aurivilius structured semiconductor consisting of an arrangement of $(WO_4)^{2-}$ layers and $(Sb_2O_2)^{2+}$ layers [16]. It has a large visible light response range and very good electrical conductivity, so it has been well studied in the field of visible light photocatalysis [17]. More importantly, the band structure of Sb_2WO_6 is conducive to matching with g-C_3N_4, which is conducive to the construction of Sb_2WO_6/g-C_3N_4 heterojunction [18], thus improving the photocatalytic activity. For the study of Sb_2WO_6/g-C_3N_4 heterojunction, Ren et al. formed S-scheme heterojunction between spherical granular Sb_2WO_6 and sheet g-C_3N_4 by ultrasonic-assisted method, which could remove more than 68 % of continuous flowing NO within 30 minutes [19]. The spherical granular material leads to small contact surface, which reduces the catalytic activity of the photocatalyst [20]. In contrast, 2D/2D heterojunction materials have a larger contact area and can provide more charge transfer channels [21,22]. For example, Ren et al. combined iron-doped two-dimensional g-C_3N_4 with two-dimensional Bi_2MoO_6 to prepare a Z-scheme heterojunction Fenton catalyst, which improved the degradation efficiency of tetracycline hydrochloride [23]. zhang et al. synthesized 2D/2D $Bi_4O_5I_2$/Sb_2WO_6 heterojunction to improve the photocatalytic degradation of tetracycline hydrochloride [24]. However, the suitability and performance of the 2D/2D Sb_2WO_6/g-C_3N_4 Z-scheme heterojunction with respect to photocatalytic degradation are not well known.

Herein, a surfactant, cetyltrimethylammonium ammonium bromide (CTAB), is used to synthesize dispersible sheets SWO, which are then loaded on CN by electrostatic adsorption to form the SWO/CN Z-scheme heterostructure. The photocatalytic degradation experiments of RhB and MBT show that SWO/CN delivers better degradation performance than individual Sb_2WO_6 and g-C_3N_4. The enhanced photocatalytic activity stems from the efficient separation of photogenerated carriers, and free radical trapping experiments and ESR demonstrate the vital roles of holes (h^+), superoxide ($\cdot O_2^-$), and singlet oxygen ($^1O_2$) in the catalytic degradation process.

2. Experimental details

2.1. Reagents and materials

Urea (CH_4N_2O, AR), sodium tungstate dihydrate ($Na_2WO_4 \cdot 2H_2O$, 99.5 %), 1,4-benzoquinone (BQ, AR), cetyltrimethylammonium bromide (CTAB, 99.0 %), L-tryptophan, triethanolamine (TEOA, AR), anhydrous ethanol (99.7 %), 2-mercaptobenzothiazole (MBT), and rhodamine B (RhB, AR) were purchased from the National Pharmaceutical Reagent. Antimony chloride ($SbCl_3$, AR) was purchased from Aladdin.

2.2. Sample preparation

Preparation of Sb_2WO_6: A solution containing 0.228 g of antimony chloride in 18 mL of H_2O was prepared and stirred for 15 min, followed by the addition of 2 mL of hydrochloric acid. 0.165 g of sodium tungstate dihydrate and 0.05 g of cetyltrimethylammonium bromide were introduced to a beaker containing 20 mL of H_2O and stirred for 15 min. These two solutions were then combined, transferred to a 50 mL hydrothermal reactor, and heated for 24 h to 140 °C. The Sb_2WO_6 catalyst was obtained by washing three times with water and alcohol and drying.

Preparation of g-C_3N_4: Urea (6 g) was placed in a crucible, and argon was bled into the tube furnace. The temperature was raised to 550°C at a rate of 2.2 °C/min for a period of 4 hours. The product was cleaned to form g-C_3N_4.

Preparation of SWO/CN: The prepared Sb_2WO_6 was placed in a beaker containing 40 mL of ethanol and sonicated for 1 h. The prepared g-C_3N_4 was weighed, put in the above solution, and sonicated for 1 h. The X% Sb_2WO_6/g-C_3N_4 (X = 20, 30, 40, and 50) catalysts were obtained by stirring ultrasonically for 20 h, filtering, washing, and drying. The samples were designated 20 % SWO/CN, 30 % SWO/CN, and 40 % SWO/CN, and 50 % SWO/CN based on the ratio of Sb_2WO_6 to g-C_3N_4. The fabrication process is illustrated schematically in Scheme 1.

2.3. Characterization

An electrochemical workstation (CHI660B) was used to monitor the photocurrents and perform electrochemical impedance spectroscopy (EIS). X-ray photoelectron spectroscopy (XPS) was conducted on the ESCALAB QXi, and the morphology was examined on the JEOL JEM-2010 transmission electron microscope (TEM) and JSM-7800F scanning electron microscope (SEM). X-ray diffraction was carried out on the Shimadzu XRD-6100, and atomic force microscopy (AFM) was performed on the Bruker Innova. The degradation pathways were analyzed by liquid chromatography-mass spectrometry on the Q Extractive Plus.

2.4. Photocatalytic activity

10 mg/L RhB and MBT were degraded to evaluate the photodegradation properties of the SWO/CN materials for the treatment of

organic pollutants. The sample (50 mg) was degraded in 50 mL of 10 mg/L RhB/MBT and then dispersed ultrasonically. A 250 W xenon lamp and UV cut-off filter with a wavelength cutoff of 400 nm or greater were employed as the visible light source. To maintain the temperature at 25°C, a thermostatic circulating water system was employed. At intervals of 0.5 h, 3 mL of the solution were removed and centrifuged. The concentration of the product in the solution was determined by UV-Vis spectrophotometry. The kinetic constant, K, of the quasi-first-order reaction is calculated by the following formula:

$$-kt = \ln\frac{C_t}{C_0}$$

where C_0 represents the contaminant level after the 30-minute dark reaction and C_t denotes the contaminant concentration at a given time point under light irradiation.

3. Results and discussion

3.1. Structure

The assembly of Sb_2WO_6 nanosheets and g-C_3N_4 nanosheets was achieved by adding Sb_2WO_6 to the g-C_3N_4 solution and mixing it thoroughly under continuous agitation. In order to confirm the success of electrostatic self-assembly of SWO/CN heterostructure, the zeta potentials of Sb_2WO_6 nanosheets and g-C_3N_4 nanosheets were measured [25]. As shown in Figure S1, the prepared g-C_3N_4 nanosheets are negatively charged with a zeta potential of −31 mV. When the positively charged Sb_2WO_6 (11 mV) was mixed with the negatively charged g-C_3N_4, the Sb_2WO_6 nanosheet was immobilized on the g-C_3N_4 nanosheet by electrostatic interaction. The opposite potential can cause electrostatic attraction between them, thus forming a stable heterostructure.

The structure of Sb_2WO_6, g-C_3N_4 and X% SWO/CN is determined by XRD (X-ray diffraction) (Fig. 1**a**). The peaks at 13.1° and 27.4° arise from the (002) and (100) planes of g-C_3N_4, respectively. This is due to the ordered arrangement of the 3-s-triazine units and the stacking of the conjugated aromatic rings in the plane of g-C_3N_4 [26]. The diffraction peaks at 26.83°, 29.16°, 32.78°, 36.46°, 40.23°, 47.33°, 49.81°, 53.28°, and 55.40° represent the (211), (002), (310), (320), (041) and (322), (051), (033), and (501) planes of SWO (JCPDS No:50–1553) [27]. The XRD diffraction peaks of the heterojunction do not shift compared to Sb_2WO_6 and g-C_3N_4, indicating that the composites of Sb_2WO_6 and g-C_3N_4 have a similar crystalline structure. The functional groups in g-C_3N_4, Sb_2WO_6, and X% SWO/CN composites are analyzed by Fourier transform infrared spectroscopy (FTIR). The X% SWO/CN composites exhibit infrared spectral features similar to Sb_2WO_6 and g-C_3N_4 (Fig. 1**b**). In Sb_2WO_6, the peaks of Sb_2WO_6 between 442 and 721 cm^{-1} are stretching vibrations of W-O, Sb-O, and W-O-W [28]. The peak of g-C_3N_4 at 1638 cm^{-1} is C═N stretching, those at 1240 cm^{-1}, 1319 cm^{-1}, 1408 cm^{-1}, 1454 cm^{-1}, and 1572 cm^{-1} are aromatic C-N stretching vibrations [29], and the peak at 3244 cm^{-1} corresponds to N-H stretching. The results indicate that X% SWO/CN heterojunctions have been successfully prepared by the electrostatic self-assembly technique.

The chemical states are determined by X-ray photoelectron spectroscopy (XPS). As shown in Fig. 1**c**, the Sb 3*d* spectra of the composite 40 % SWO/CN and Sb_2WO_6 can be fitted by two peaks at 539.6 eV and 530.2 eV, respectively [30]. The peaks in the W 4 *f* spectrum at 37.1 eV and 35.1 eV are associated with W^{6+} (Fig. 1**d**), while those at 35.3 and 33.6 eV are related to W^{5+} [31]. The peak in the O 1 *s* spectrum at 529.9 eV for both Sb_2WO_6 and 40 % SWO/CN samples represents W-O, and that at 530.7 eV stems from Sb-O (Fig. 1**e**) [32]. The N 1 *s* spectrum shows three peaks at 401.4 eV, 399.9 eV, and 398.7 eV (Fig. 1**f**). The peak at 398.7 eV arises from sp^2-bonded nitrogen (C-N-C) and that at 399.9 eV indicates the formation of a tertiary nitrogen-carbon bond (N-$(C)_3$). The amino group (C-N-H) is shown at 401.4 eV [33]. The binding energies of the C 1 *s*, O l*s*, Sb 3*d*, and W 4 *f* peaks in 40 % SWO/CN shift slightly compared to the pure components due to the electron shielding effect and change in the electron density. The results indicate a strong interfacial effect between Sb_2WO_6 and g-C_3N_4 in 40 % SWO/CN and corroborate the successful synthesis of the SWO/CN heterojunction.

3.2. Morphology

The morphology is examined by transmission electron microscopy (TEM) and scanning electron microscope (SEM). It can be seen from the figure that Sb_2WO_6 and g-C_3N_4 are in sheet structure (Figure S3a and S3b). In the composite, the Sb_2WO_6 sheet is loaded on the g-C_3N_4 sheet (Figure S3c-**f**). The ultrathin wrinkled g-C_3N_4 lamellar structure is synthesized by etching with argon during the calcination process (Fig. 2**a**). The TEM image of Sb_2WO_6 shows irregularly stacked thin sheets (Fig. 2**b**). The Sb_2WO_6 nanosheets are smaller than g-C_3N_4, enabling them to be distributed on g-C_3N_4. Fig. 2**c** shows that Sb_2WO_6 (211) has a

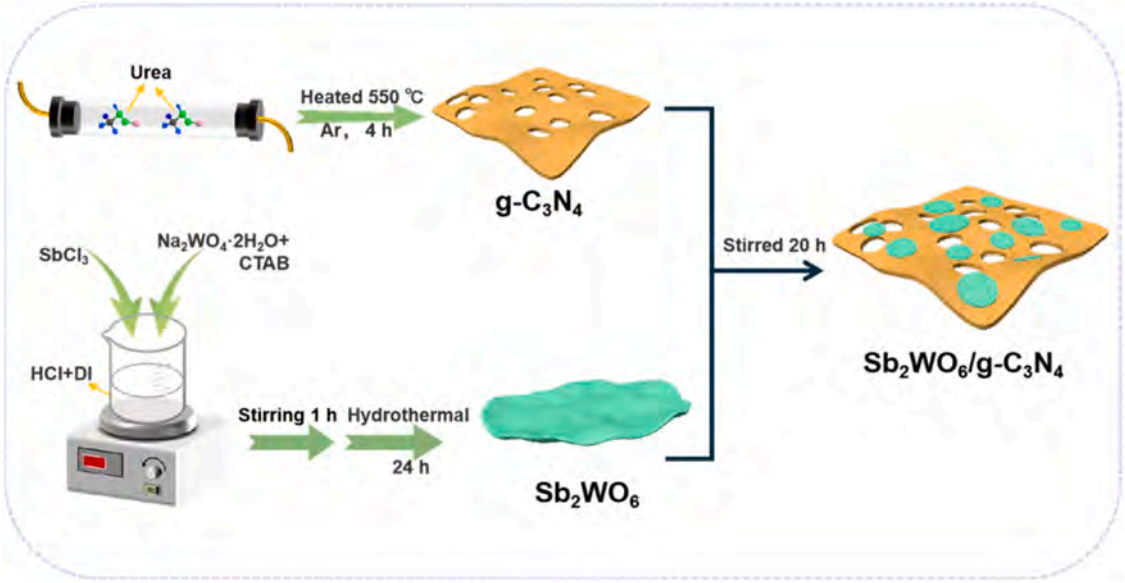

Scheme 1. Schematic of the synthesis of SWO/CN.

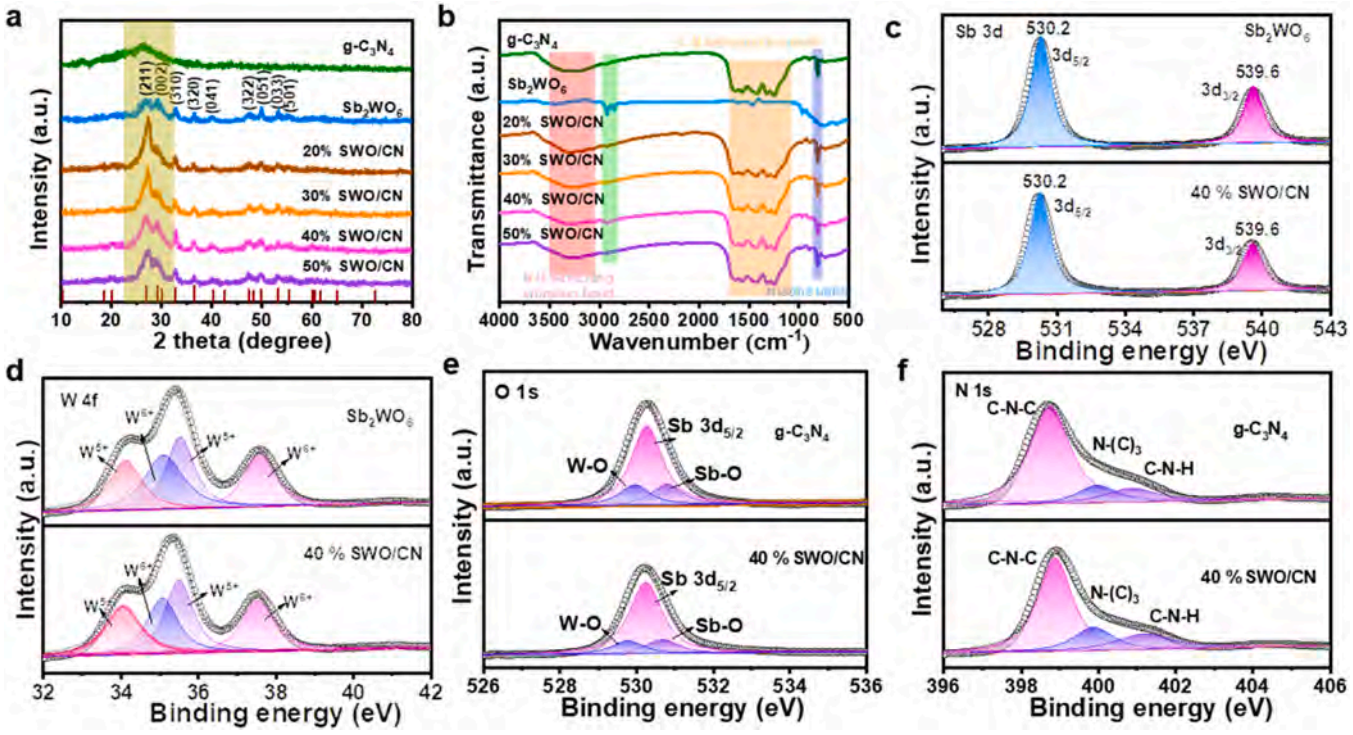

Fig. 1. (a) XRD spectra; (b) FTIR spectra; XPS spectra of (c) Sb 3*d*, (d) W 4 *f*, (e) O 1 *s*, and (f) N 1 *s*.

spacing of 0.33 nm. In the TEM image of 40 % SWO/CN, g-C_3N_4 as the substrate is lighter at the bottom, and the thick Sb_2WO_6 is darker at the top and is evenly distributed on the former (Fig. 2**d**). In the TEM image of 40 % SWO/CN, the interface between Sb_2WO_6 and g-C_3N_4 is demarcated by an orange curve, and the local image is enlarged to mark the size of the lattice spacing (Figs. 2**e and** 2**f**). Fig. 2**g** shows the high angle annular dark field (HAADF-STEM) plot of 40 % SWO/CN, and C, N, Sb, W, and O are uniformly distributed throughout the composite.

The content of each element in the synthetic samples was tested using ICP and elemental analysis (EA) (Table S2), respectively. It can be concluded from the table that the nitrogen (N) and oxygen (O) contents are high, and the metal (Sb and W) contents are low, which may be caused by part of Sb_2WO_6 not loaded on g-C_3N_4. There is little difference between the element content ratio and the calculated theoretical value. The thickness of 40 % SWO/CN is determined by atomic force microscopy (AFM) (Figure S4). The lamellar Sb_2WO_6 is tightly bound to g-C_3N_4, and the thicknesses of g-C_3N_4 and Sb_2WO_6 on the bottom layer are about 14.3 nm and 9.7 nm, respectively, indicating a compact interface.

3.3. Photochemical and electrochemical properties

The surface area affects the photocatalytic properties and is derived from the nitrogen adsorption and desorption isothermal curves. As shown in Fig. 3**a**, the specific surface area of 40 % SWO/CN is 39.1703 m^2/g, which is almost equal to those of g-C_3N_4 (36.8846 m^2/g) and Sb_2WO_6 (35.0617 m^2/g). The light absorption capacity is another essential factor and is evaluated by UV–vis DRS. The edge of the absorption band of X% SWO/CN is about 450 nm (Fig. 3**b**), and there is strong absorption in the visible region. The absorption bands of Sb_2WO_6 and g-C_3N_4 are at 520 nm and 450 nm, respectively. As shown in the upper right inset in Fig. 3**b**, according to the equation $ah\nu=A(h\nu-E_g)^{n/2}$, the bandgaps of Sb_2WO_6 and g-C_3N_4 are 2.02 eV and 2.60 eV, respectively [34]. Mott-Schottky evaluation is carried out on Sb_2WO_6 and g-C_3N_4 on the electrochemical workstation to determine the energy bands. The tangent slope of the Mott-Schottky curves of g-C_3N_4 and Sb_2WO_6 is positive (Fig. 3**c**), revealing that the catalysts are N-type semiconductors with flat band potentials of −1.17 V and −0.32 V, respectively (vs. Ag/AgCl (pH = 6.8)) [35]. According to the formula: $E_{fb} = E_{Ag/AgCl} + 0.059\ pH + E^0_{Ag/AgCl}$ [36], the standard hydrogen electrode potentials (E_{fb}) of Sb_2WO_6 and g-C_3N_4 are + 0.32 V and −0.57 V vs. NHE. For N-type semiconductors, where E_{CB} is typically negative 0–0.3 eV over E_{fb} [16], the calculated E_{CB} values of Sb_2WO_6 and g-C_3N_4 are equivalent to −0.02 V and −0.87 V vs. NHE. The E_{VB} value of a semiconductor can be calculated by $E_g = E_{VB} - E_{CB}$. The E_{VB} values of Sb_2WO_6 and g-C_3N_4 are 2.00 V and 1.73 V vs. NHE, respectively. The schematic diagram of the energy band structure is depicted in Fig. 3**d.** The valence and conduction bands of Sb_2WO_6 and g-C_3N_4 favor the formation of Z-scheme heterojunctions.

Charge carrier migration and separation efficiency are the key factors affecting the catalytic properties. Fig. 3**e** shows the electrochemical impedance spectra of carbon nitride, Sb_2WO_6, and 40 % SWO/CN. A smaller semi-circular arc indicates that the photogenerated carrier transfer efficiency is higher with smaller resistance [37]. Meanwhile, the transient photocurrent response and the photocurrent response of 40 % SWO/CN are greater (Fig. 3**f**), revealing excellent electron migration [38]. The 40 % SWO/CN photocatalyst shows better carrier migration and less recombination.

3.4. Photocatalytic degradation

To gauge the photolytic capability of the SWO/CN photocatalyst, RhB and MBT are decomposed under visible light irradiation. As shown in Fig. 4**a**, the catalyst is important in the photodegradation process. The degradation rate of 40 % SWO/CN is 96 % within 2 h, and degradation continues to a steady state within 2 h. The degradation rates of RhB by Sb_2WO_6 and g-C_3N_4 in 4 h are 72 % and 62 %, respectively, which were much lower than those of X% SWO/CN. The catalytic rate is evaluated by the quasi-first-order model. The rate constants (K) for RhB are shown in Fig. 4**b**. The rate constant (K) (0.0194 min^{-1}) of RhB degradation by 40 % SWO/CN was higher than that of Sb_2WO_6 (0.0054 min^{-1}) and g-C_3N_4 (0.0039 min^{-1}). In addition, a larger ratio of Sb_2WO_6 to g-C_3N_4 boosts the photodegradation rate. When the ratio increases from 20 % to

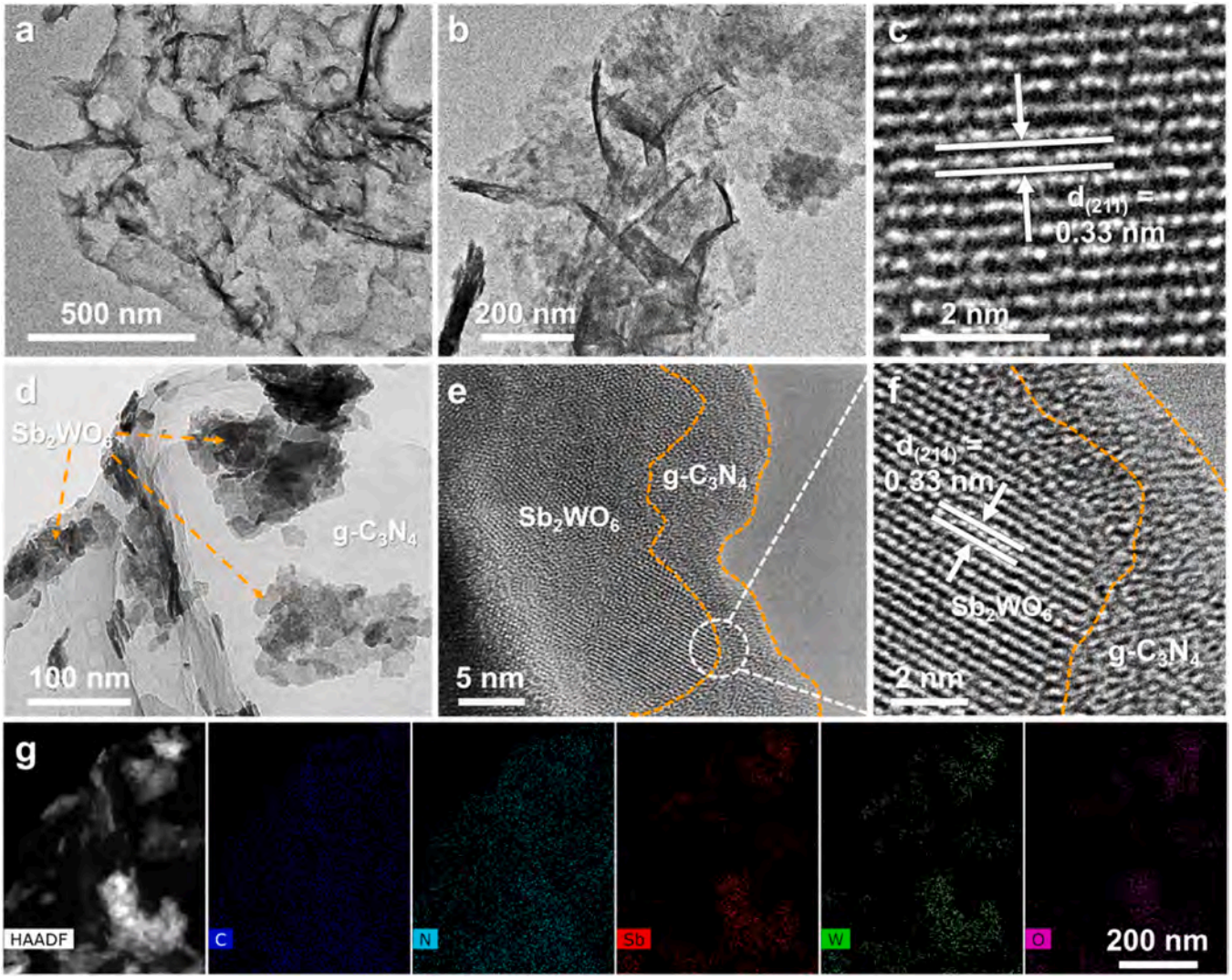

Fig. 2. TEM images of (a) g-C_3N_4 and (b) Sb_2WO_6; (c) HR-TEM image of Sb_2WO_6; (d) TEM image of SWO/CN; (e) TEM boundary diagram of SWO/CN; and (f) Enlarged view of the selected area; (g) HAADF-STEM images of SWO/CN.

40 %, the rate constant increases, but when it is 50 %, the rate starts to slow maybe due to excessive loading and reduced active site. Figure S6a shows that the degradation rate of Sb_2WO_6 for MBT is 22 % within 5 h, and that of g-C_3N_4 is 53 % for the same time. In comparison, the degradation rate of 40 % SWO/CN is 92 %. The quasi-first-order kinetics curve and the quasi-sum rate constant K indicate the degree of improvement. The degradation rate constant K of 40 % SWO/CN is 0.4391 h^{-1}, which is 2.96 and 9.32 times larger than those of g-C_3N_4 (0.1484 h^{-1}) and Sb_2WO_6 (0.0471 h^{-1}) (Figure S6b). The results show that the tightly bound 2D/2D Z-scheme heterojunctions formed by self-assembly with electrostatic attraction improve the photocatalytic activity. The photocatalytic stability is another important parameter. Fig. 4**c** reveals that 40 % SWO/CN sample experiences minimal decline in the catalytic activity after four cycles. FTIR, XRD, SEM and XPS are used to characterize the structure of the recycled materials. As shown in Figure S7 and Figure S9, the XRD and XPS spectrum of 40 % SWO/CN does not change significantly, and the peak from Sb_2WO_6 can still be observed. FTIR discloses that the chemical bonds are similar before and after cycling, thus concluding the strong structural stability. SEM was used to characterize the morphology of the samples after four cycles, and it was found that the sample morphology was almost unchanged (Figure S8).

In order to study the anti-interference ability of the photocatalyst, the photocatalytic degradation activity of RhB by 40 % SWO/CN in real water environment was simulated by ion interference experiment and at different pH values. 1 mmol/L of different kinds of inorganic salts were added into the photocatalytic system, and the influence of negative and cation on the photocatalytic reaction was determined by the control variable method. As shown in Figure S6d, after the addition of sodium salt, Cl^- and SO_4^{2-} have little effect on the photocatalytic degradation of RhB compared with the control group, while CO_3^{2-} and PO_4^{3-} have a hindrant effect on the degradation. This may be caused by its ability to trap the active free radicals produced in the photocatalyst. After the addition of chlorine salts, most of the cations had little effect on the photocatalytic degradation ability, indicating that the photocatalyst could adapt to the degradation of most of the ion-containing polluted water bodies (Figure S6e). Degradation tests were carried out at pH= 1, 4, 8, 11 and control conditions. It was found that the catalytic activity of photocatalyst decreased less under acidic conditions and remained stable. With the increase of pH value, the degree of activity decline is higher, because under alkaline conditions, RhB molecule and photocatalyst produce repulsion due to the action of free radicals (Figure S6f). The above analysis provides a certain basis for the use of photocatalyst in actual water, and provides feasible theoretical support for subsequent research.

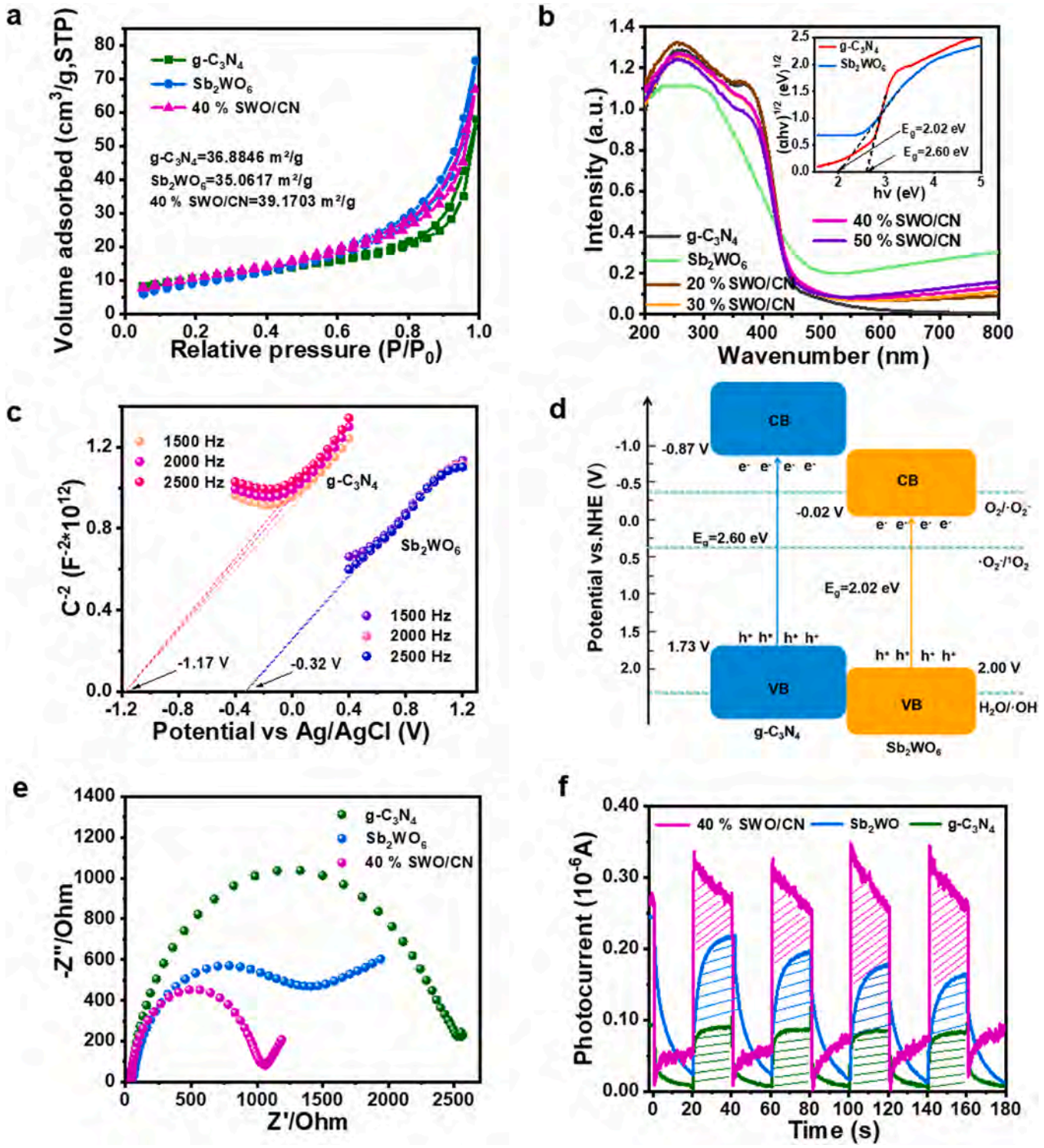

Fig. 3. (a) N_2 adsorption-desorption isotherms; (b) $(ahv)^{1/2}$ versus hv plots; (c) Mott-Schottky plots of Sb_2WO_6 and g-C_3N_4; (d) Band structure of SWO/CN; (e) Photocurrent responses; (f) Electrochemical impedance spectra.

3.5. Photocatalytic degradation mechanism

The removal of contaminants is primarily contingent upon the active species produced. Therefore, free radical trapping experiments are performed to determine which species are active during photocatalysis and also to understand how RhB is degraded. In the experiments, IPA, TEOA, L-tryptophan, and BQ are used as scavengers of ·OH, h^+, $^1O_2$, and $\cdot O_2^-$, respectively [39]. After BQ, L-tryptophan, and TEOA are added, the inhibitory effect on the catalytic degradation of RhB by 40 % SWO/CN increases, as manifested by degradation rates of 23 %, 42 %, and 19 %, respectively (Fig. 4**d**), indicating that $^1O_2$, h^+, and $\cdot O_2^-$ are the main active species. However, after the addition of IPA, the degradation activity is consistent with that of the control group with only the catalyst added, indicating that ·OH does not play a catalytic role, because ·OH is not produced by the catalytic system. The ESR spintron resonance test is conducted to identify the active species, as shown in Fig. 4**e-h**. The 1:1:1

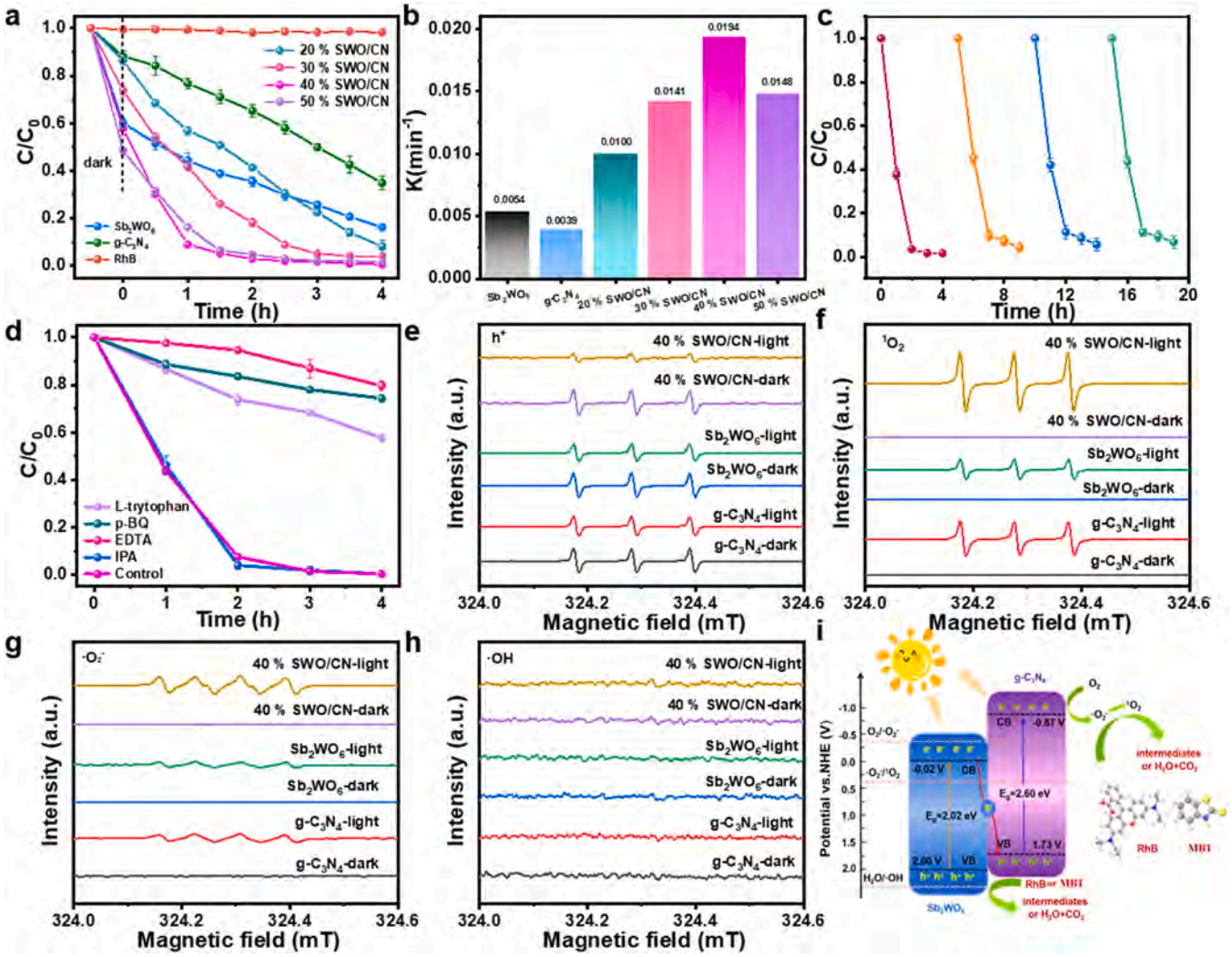

Fig. 4. (a) Degradation of RhB; (b) Pseudo-first-order rate constants; (c) Recycling experiments for RhB degradation; (d) Rapping experiment of RhB for SWO/CN; ESR spectra of (e) TEMPO-h^+, (f) DMPO-·O_2^-, (g) TMPO-$^1O_2$, and (h) DMPO-·OH adducts; (i) Mechanism of photocatalytic degradation.

signal peak corresponds to h^+ production. After irradiation, the TEMPO-h^+ signal decreases, suggesting that holes are used during degradation. Moreover, under light conditions, the TEMPO-h^+ signal intensity of 40 % SWO/CN decreases more, indicating a higher utilization of h^+ oxidation. Similarly, the peaks of 1:1:1 and 1:2:2:1 correspond to TEMP-$^1O_2$ and DMPO-·O_2^-, respectively [40]. The enhancement after illumination and the absence of the signal without illumination indicate the production of oxygen-reactive radicals. The signals of DMPO-·O_2^- and TEMP-$^1O_2$ synthesized with 40 % SWO/CN are higher than those of the monomer Sb_2WO_6 and g-C_3N_4, implying that 40 % SWO/CN can generate more $^1O_2$ and ·O_2^-. Finally, the DMPO-·OH signal of the samples does not change with or without light, indicating that there is no ·OH production in the catalytic system. The change of the signal intensity of free radicals above proves the production of active species. The results also demonstrate that the photogenerated electron transfer pathways in the SWO/CN composites satisfy the Z-scheme heterojunction scheme, but not the other heterojunction schemes.

Visible light excites Sb_2WO_6 and g-C_3N_4 to generate photogenerated electron-hole pairs. However, the accumulated electrons (e^-) on the CB of Sb_2WO_6 cannot reduce O_2 to superoxide radicals (·O_2^-). Because the potential required for ·O_2^- generation is more negative than −0.33 (O_2/·O_2^-=-0.33 eV vs. NHE) and its CB position of −0.02 eV is less negative [41,42]. Therefore, a Z-scheme photocatalytic degradation mechanism is presented in Fig. 4**i**. Electrons accumulate on the CB of g-C_3N_4 and holes accumulate on the VB of Sb_2WO_6, thus separating electron-hole pairs. Subsequently, since the conduction band potential of g-C_3N_4 is lower than the REDOX potential of O_2/·O_2^-, the dissolved O_2 in the reaction system is converted to ·O_2^- by the action of electrons. At the same time, superoxide radical (·O_2^-) and hole (h^+) can also form singlet oxygen ($^1O_2$), and then degrade organic matter into small molecular intermediates and CO_2 and H_2O [43]. Therefore, the organic matter molecules are cleaved and mineralized under the action of ·O_2^-, $^1O_2$ and h^+ active species.

3.6. Photocatalytic degradation pathways

Dye molecules may be induced to form unstable and colorless transition forms during photodegradation, rather than complete and complete mineralization [44]. Therefore, in order to explain the degradation and investigate the possible pathways, liquid chromatography-mass spectrometry (LC-MS) is performed to identify the intermediate products (Fig. 5). Under visible light illumination, deethylation of RhB occurs first, and the tetraethyl group is successively removed. The loss of the ethyl group results in the formation of N-ethyl rhodamine (m/z = 359) and rho rhodamine 110 (m/z = 331). The REDOX reactions follow, and the intermediates are mineralized into small molecules of CO_2 and H_2O.

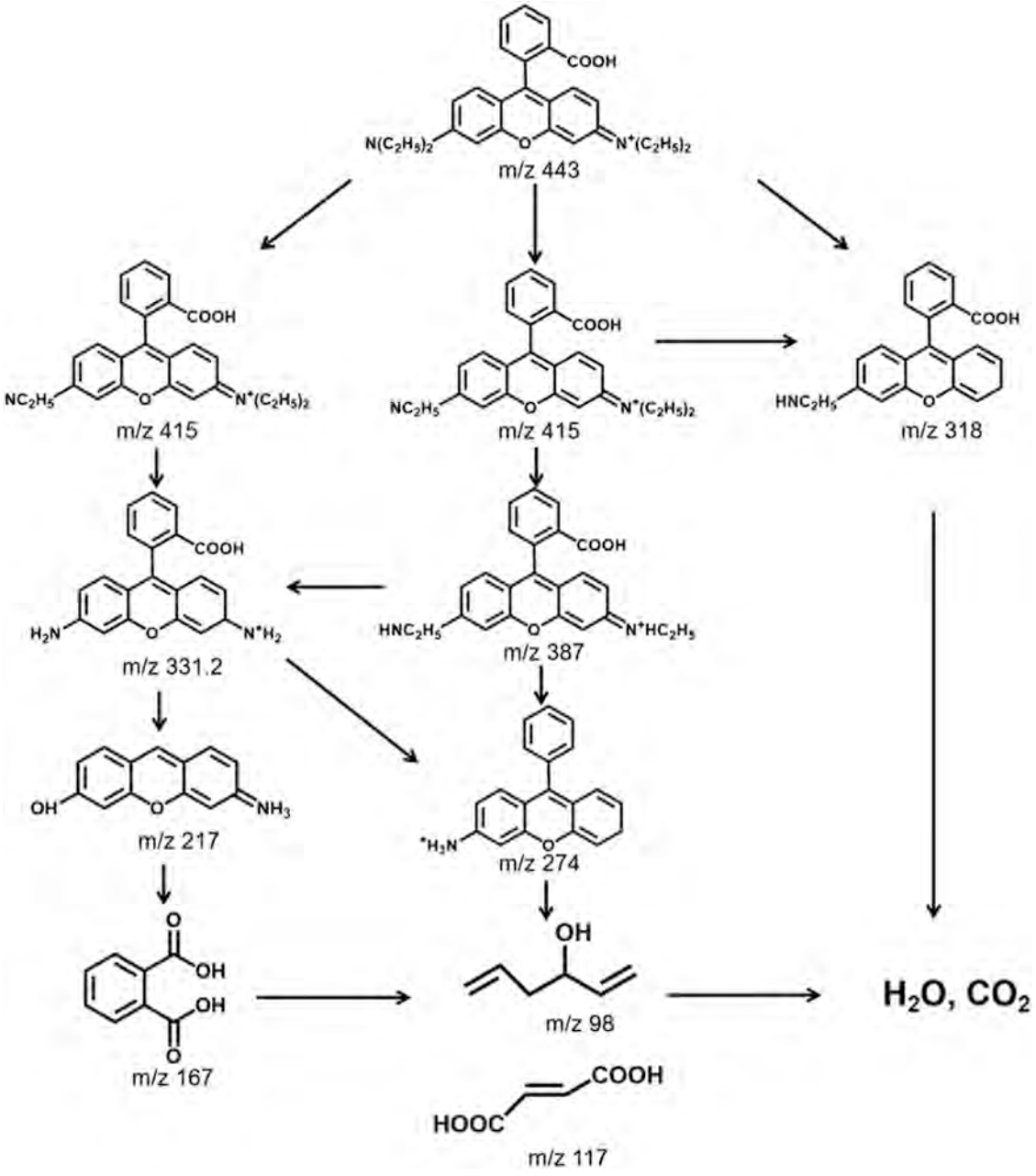

Fig. 5. RhB potential degradation pathways based on LC-MS.

4. Conclusion

Z-scheme SWO/CN heterojunction photocatalysts are prepared by hydrothermal and electrostatic adsorption methods. In the composite catalysts, photogenerated holes and electrons are more easily separated and have strong oxidizing and reducing capabilities. Photodegradation of RhB by 40 % SWO/CN is 5 times and 3.6 times faster than those of g-C_3N_4 and Sb_2WO_6, and $^1O_2$, $\cdot O_2^-$, and h^+ play important roles in the degradation of pollutants. This study reveals a feasible strategy for high-performance pollutant degradation.

CRediT authorship contribution statement

Liu Jinyuan: Writing – review & editing, Writing – original draft, Data curation, Conceptualization. **Peng Qichang:** Writing – review & editing, Formal analysis, Data curation. **Liu Jinxin:** Writing – review & editing, Writing – original draft, Methodology, Formal analysis, Data curation, Conceptualization. **Gao Xue:** Writing – review & editing, Formal analysis, Data curation. **Li Huaming:** Writing – review & editing, Supervision, Resources, Investigation. **Wang Bin:** Writing – review & editing, Funding acquisition, Formal analysis, Data curation. **Zhu Xingwang:** Writing – review & editing, Methodology, Formal analysis, Conceptualization. **Xu Hui:** Writing – review & editing, Supervision, Resources, Funding acquisition. **Chu Paul K.:** Writing – review & editing, Supervision, Funding acquisition, Formal analysis.

Declaration of Competing Interest

The authors declare that they have no known competing financial interests or personal relationships that could have appeared to influence the work reported in this paper.

Acknowledgments

This work was financially supported by the National Natural Science Foundation of China (No. 22108106, 22308300), Natural Science Foundation of Jiangsu Province (No. BK20220598), Key Laboratory of Electrochemical Energy Storage and Energy Conversion of Hainan Province (No. KFKT2024005), and City University of Hong Kong Donation Research Grants (DON-RMG No. 9229021 and 9220061).

Appendix A. Supporting information

Supplementary data associated with this article can be found in the online version at doi:10.1016/j.colsurfa.2025.136342.

Data Availability

Data will be made available on request.

References

[1] R. Yang, Y. Fan, J. Hu, Z. Chen, H.S. Shin, D. Voiry, Q. Wang, Q. Lu, J.C. Yu, Z. Zeng, Photocatalysis with atomically thin sheets, Chem. Soc. Rev. 52 (2023) 7687–7706, https://doi.org/10.1039/D2CS00205A.

[2] B. Wang, W. Zhang, G. Liu, H. Chen, Y. Weng, H. Li, P.K. Chu, J. Xia, Excited electron-rich $Bi^{(3-x)+}$ sites: a quantum well-like structure for highly-promoted selective photocatalytic CO_2 reduction performance, Adv. Funct. Mater. 32 (2022) 202202885, https://doi.org/10.1002/adfm.202202885.

[3] P.V. Kamat, Semiconductor surface chemistry as holy grail in photocatalysis and photovoltaics, Acc. Chem. Res. 50 (2017) 527–531, https://doi.org/10.1021/acs.accounts.6b00528.

[4] S. Dong, Y. Gong, Z. Zeng, S. Chen, J. Ye, Z. Wang, D.D. Dionysiou, Dissolved organic matter promotes photocatalytic degradation of refractory organic pollutants in water by forming hydrogen bonding with photocatalyst, Water Res. 242 (2023) 120297, https://doi.org/10.1016/j.watres.2023.120297.

[5] S. Zhu, Q. Ruan, X. Zhu, D. Li, B. Wang, C. Huang, L. Liu, F. Xiong, J. Yi, Y. Song, J. Liu, H. Li, P.K. Chu, H. Xu, Co single atom coupled oxygen vacancy on $W_{18}O_{49}$ nanowires surface to construct asymmetric active site enhanced peroxymonosulfate activation, J. Colloid Interface Sci. 664 (2024) 736–747, https://doi.org/10.1016/j.jcis.2024.02.166.

[6] Y. Wen, A. Renteria-Gomez, G.S. Day, M.F. Smith, T. Yan, R. Ozdemir, O. Gutierrez, V.K. Sharma, X. Ma, H. Zhou, Integrated photocatalytic reduction and oxidation of perfluorooctanoic acid by metal-organic frameworks: key insights into the degradation mechanisms, J. Am. Chem. Soc. 144 (2022) 11840–11850, https://doi.org/10.1021/jacs.2c04341.

[7] B. Wang, H. Chen, W. Zhang, H. Liu, Z. Zheng, F. Huang, J. Liu, G. Liu, X. Yan, Y. Weng, H. Li, Y. She, P.K. Chu, J. Xia, Semimetallic bismuthene with edge-rich dangling bonds: broad-spectrum-driven and edge-confined electron enhancement boosting CO_2 hydrogenation reduction, Adv. Mater. 36 (2024) 2312676, https://doi.org/10.1002/adma.202312676.

[8] F. Saadati, N. Keramati, M.M. Ghazi, Influence of parameters on the photocatalytic degradation of tetracycline in wastewater: a review, Crit. Rev. Environ. Sci. Technol. 46 (2016) 757–782, https://doi.org/10.1080/10643389.2016.1159093.

[9] W. Qian, S. Xu, X. Zhang, Differences and similarities of photocatalysis and electrocatalysis in two-Dimensional nanomaterials: strategies, traps, applications and challenges, Nano-Micro Lett. (2021) 156, https://doi.org/10.1007/s40820-021-00681-9.

[10] G. Liu, C. Zhen, Y. Kang, L. Wang, H. Cheng, Unique physicochemical properties of two-dimensional light absorbers facilitating photocatalysis, Chem. Soc. Rev. 47 (2018) 6410–6444, https://doi.org/10.1039/C8CS00396C.

[11] J. Yang, K. Yanga, X. Zhu, Z. Wang, Z. Yang, X. Ding, K. Zhong, M. He, H. Li, H. Xu, Band engineering of non-metal modified polymeric carbon nitride with broad spectral response for enhancing photocatalytic CO2 reduction, Chem. Eng. J. 461 (2023) 141841, https://doi.org/10.1016/j.cej.2023.141841.

[12] L. Li, H. Liu, C. Cheng, X. Dai, F. Chen, J. Ning, W. Wang, Y. Hu, Photochemical tuning of tricoordinated nitrogen deficiency in carbon nitride to create delocalized π electron clouds for efficient CO_2 photoreduction, ACS Catal. 14 (2024) 10204–10213, https://doi.org/10.1021/acscatal.4c01636.

[13] A. Mehtab, T. Ahmad, Unveiling the bifunctional photo/electrocatalytic activity of in situ grown CdSe QDs on g-C_3N_4 Nanosheet Z-Scheme Heterostructures for Efficient Hydrogen Generation, ACS Catal. 14 (2024) 691–702, https://doi.org/10.1021/acscatal.3c03632.

[14] D. Zhao, Y. Wang, C. Dong, Boron-doped nitrogen-deficient carbon nitride-based Z-scheme heterostructures for photocatalytic overall water splitting, Nat. Energy 6 (2021) 388–397, https://doi.org/10.1038/s41560-021-00795-9.

[15] B. Wang, J. Zhao, H. Chen, Y. Weng, H. Tang, Z. Chen, W. Zhu, J. Xia, H. Li, Unique Z-scheme carbonized polymer dots/$Bi_4O_5Br_2$ hybrids for efficiently boosting photocatalytic CO_2 reduction, Appl. Catal. B. 293 (2021) 120182, https://doi.org/10.1016/j.apcatb.2021.120182.

[16] W. Li, Z. Wang, Y. Li, J.B. Ghasemi, J. Li, G. Zhang, Visible-NIR light-responsive 0D/2D CQDs/Sb_2WO_6 nanosheets with enhanced photocatalytic degradation performance of RhB: Unveiling the dual roles of CQDs and mechanism study, J. Hazard. Mater. 424 (2022) 127595, https://doi.org/10.1016/j.jhazmat.2021.127595.

[17] Q. Peng, Q. Ruan, B. Wang, J. Liu, C. Huang, X. Zhu, D. Li, L. Liu, Y. Wang, X. Zhang, P.K. Chu, H. Xu, Low-temperature plasma-induced porous Sb_2WO_6 microspheres with rich oxygen vacancies to promote high-performance photocatalytic activity, Colloid Surf. A 681 (2024) 132724, https://doi.org/10.1016/j.colsurfa.2023.132724.

[18] Z. Wang, Y. Li, Q. Cheng, X. Wang, J. Wang, G. Zhang, Sb-based photocatalysts for degradation of organic pollutants: a review, J. Clean. Prod. 367 (2022) 133060, https://doi.org/10.1016/j.jclepro.2022.133060.

[19] Y. Ren, Y. Li, X. Wu, J. Wang, G. Zhang, S-scheme Sb_2WO_6/g-C_3N_4 photocatalysts with enhanced visible-light-induced photocatalytic NO oxidation performance, Chin. J. Catal. 42 (2021) 69–77, https://doi.org/10.1016/S1872-2067(20)63631-2.

[20] S. Cao, X. Xu, Q. Liu, H. Zhu, T. Hu, Sulfur vacancies and heterogeneous interfaces promote high performance sodium storage of bimetallic chalcogenide hollow nanospheres, J. Energy Chem. 95 (2024) 596–610, https://doi.org/10.1016/j.jechem.2024.04.013.

[21] Y. Zhang, F. Cao, S. Zhao, J. Zhang, S. Zhong, H. Mao, L. Zhao, S. Bai, Efficient charge and proton balance enabled by a 2D/2D S-scheme heterojunction with a nanochamber design for better synergy of photocatalytic CO_2 methanation and benzylamine oxidation, Adv. Funct. Mater. (2024) 2413830, https://doi.org/10.1002/adfm.202413830.

[22] G. Yan, X. Sun, Y. Zhang, H. Li, H. Huang, B. Jia, D. Su, T. Ma, Metal-Free 2D/2D van der Waals heterojunction based on covalent organic frameworks for highly efficient solar energy catalysis, Nano-Micro Lett. 15 (2023) 132, https://doi.org/10.1007/s40820-023-01100-x.

[23] G. Ren, J. Zhang, S. Li, L. Zhang, C. Shao, X. Wang, H. Bai, Z-scheme heterojunction composed of Fe-doped g-C_3N_4 and Bi_2MoO_6 for photo-fenton degradation of antibiotics over a wide pH range: activity and toxicity assessment, Environ. Res. 252 (2024) 118886, https://doi.org/10.1016/j.envres.2024.118886.

[24] Y. Zhang, H. Liua, J. Peng, J. Guo, Li Ding, X. Cao, Yu Chang, W.B. Soltan, G. Liu, Synthesis of $Bi_4O_5I_2$ coupled with Sb_2WO_6 boosts the photocatalytic degradation of tetracyclines under simulated sunlight, J. Environ. Chem. Eng. 12 (2024) 111548, https://doi.org/10.1016/j.jece.2023.111548.

[25] P. Zhang, D. Wang, Q. Zhu, N. Sun, F. Fu, B. Xu, Plate-to-layer Bi_2MoO_6/Mxene-heterostructured anode for lithium-ion batteries, Nano-Micro Lett. 11 (2019) 81, https://doi.org/10.1007/s40820-019-0312-y.

[26] Y. Wang, C. Ban, Y. Feng, J. Ma, J. Ding, X. Wang, L. Ruan, Y. Duan, M.G. Brik, L. Gan, X. Zhou, Unveiling the synergistic role of nitrogen vacancies and Z-scheme heterojunction in g-C_3N_4/β-Bi_2O_3 hybrids for enhanced CO_2 photoreduction, Nano Energy 124 (2024) 109494, https://doi.org/10.1016/j.nanoen.2024.109494.

[27] U. Rafiq, O. Mehraj, S. Lone, Solvothermal synthesis of Ag_2WO_4/Sb_2WO_6 heterostructures for enhanced charge transfer properties and efficient visible-light-driven photocatalytic activity and stability, J. Environ. Chem. Eng. 8 (2020) 104301, https://doi.org/10.1016/j.jece.2020.104301.

[28] Y. Zhang, H. Liu, J. Peng, J. Guo, L. Ding, X. Cao, Y. Chang, W.B. Soltan, G. Liu, Synthesis of $Bi_4O_5I_2$ coupled with Sb_2WO_6 boosts the photocatalytic degradation of tetracyclines under simulated sunlight, J. Environ. Chem. Eng. 12 (2024) 111548, https://doi.org/10.1016/j.jece.2023.111548.

[29] J. Huang, Y. Cao, H. Wang, H. Yu, F. Peng, H. Zou, Z. Liu, Revealing active-site structure of porous nitrogen-defected carbon nitride for highly effective photocatalytic hydrogen evolution, Chem. Eng. J. 373 (2019) 687–699, https://doi.org/10.1016/j.cej.2019.05.088.

[30] X. Jia, Z. Yu, F. Liu, H. Liu, D. Zhang, E.C. d Santos, H. Zheng, Y. Hashimoto, Y. Chen, L. Wei, H. Li, Identifying stable electrocatalysts initialized by DataMining: Sb_2WO_6 for oxygen reduction, Adv. Sci. 11 (2024) 2305630, https://doi.org/10.1002/advs.202305630.

[31] Y. Shi, H. Wang, Z. Wang, Pt decorated hierarchical Sb_2WO_6 microspheres as a surface functionalized photocatalyst for the visible-light-driven reduction of nitrobenzene to aniline, J. Mater. Chem. A 8 (2020) 18755–18766, https://doi.org/10.1039/D4TA04514A.

[32] Y. Wang, K. Wang, J. Wang, X. Wu, G. Zhang, Sb_2WO_6/BiOBr 2D nanocomposite S-scheme photocatalyst for NO removal, J. Mater. Sci. Technol. 56 (2020) 236–243, https://doi.org/10.1016/j.jmst.2020.03.039.

[33] M.K. Hussien, A. Sabbah, M. Qorbani, R. Putikam, S. Kholimatussadiah, D.M. Tzou, M.H. Elsayed, Y. Lu, Y. Wang, X. Lee, T. Lin, N.Q. Thang, H. Wu, S. Haw, K.C. W. Wu, M. Lin, K. Chen, L. Chen, Constructing B-N-P bonds in ultrathin holey g-C_3N_4 for regulating the local chemical environment in photocatalytic CO_2 reduction to CO, Small (2024) 2400724, https://doi.org/10.1002/smll.202400724.

[34] L. Chen, Y. Chao, X. Li, G. Zhou, Q. Lu, M. Hua, H. Li, X. Ni, P. Wu, W. Zhu, Engineering a tandem leaching system for the highly selective recycling of valuable metals from spent Li-ion batteries, Green. Chem. 23 (2021) 2177–2184, https://doi.org/10.1039/d0gc03820b.

[35] G. Liu, L. Wang, X. Chen, X. Zhu, B. Wang, X. Xu, Z. Chen, W. Zhu, H. Li, J. Xia, Crafting of plasmonic Au nanoparticles coupled ultrathin BiOBr nanosheets heterostructure: steering charge transfer for efficient CO_2 photoreduction, Green. Chem. Eng. 3 (2022) 157–164, https://doi.org/10.1016/j.gce.2021.11.007.

[36] X. Hu, J. Wang, J. Wang, Y. Deng, H. Zhang, T. Xu, W. Wang, β particles induced directional inward migration of oxygen vacancies: surface oxygen vacancies and interface oxygen vacancies synergistically activate PMS, Appl. Catal. B Environ. 318 (2022) 121879, https://doi.org/10.1016/j.apcatb.2022.121879.

[37] J. Dong, J. Zhao, X. Yan, L. Li, G. Liu, M. Ji, B. Wang, Y. She, H. Li, J. Xia, Construction of carbonized polymer dots/potassium doped carbon nitride

nanosheets Van der Waals heterojunction by ball milling method for facilitating photocatalytic CO2 reduction performance in pure water, Appl. Catal. B Environ. 351 (2024) 123993, https://doi.org/10.1016/j.apcatb.2024.123993.

[38] Y. Wang, J. Hu, T. Ge, F. Chen, Y. Lu, R. Chen, H. Zhang, B. Ye, S. Wang, Y. Zhang, T. Ma, H. Huang, Gradient cationic vacancies enabling inner-to-outer tandem homojunctions: strong local internal electric field and reformed basic sites boosting CO_2 photoreduction, Adv. Mater. 35 (2023) e2302538, https://doi.org/10.1002/adma.202302538.

[39] H. Wang, D. Yong, S. Chen, S. Jiang, X. Zhang, W. Shao, Q. Zhang, W. Yan, B. Pan, Y. Xie, Oxygen-vacancy-mediated exciton dissociation in BiOBr for boosting charge-carrier-involved molecular oxygen activation, J. Am. Chem. Soc. 140 (2018) 1760–1766, https://doi.org/10.1021/jacs.7b10997.

[40] Z. Zhang, J. Liang, W. Zhang, M. Zhou, X. Zhu, Z. Liu, Y. Li, Z. Guan, C. Lee, P. K. Wong, H. Li, Z. Jiang, Modified-pollen confined hybrid system: a promising union for visible-light-driven photocatalytic antibiotic degradation, Appl. Catal. B. 330 (2023) 122621, https://doi.org/10.1016/j.apcatb.2023.122621.

[41] Q. Liu, Z. Yu, D. Liang, J. Xiong, T. Gan, H. Hu, Z. Huang, Y. Zhang, Elemental imprinting-induce dinterfacial growth strategy to bridge g-C_3N_4 and Bi_2MoO_6 with engineering rapid electron transfer pathway for efficient visible light-driven photocatalysis, Chem. Eng. J. 496 (2024) 154057, https://doi.org/10.1016/j.cej.2024.154057.

[42] F. Opoku, K.K. Govender, C.G.C.E. Sittert, P.P. Govender, Insights into the photocatalytic mechanism of mediator-free direct Z-scheme g-C_3N_4/Bi_2MoO_6(010) and g-C_3N_4/Bi_2WO_6(010) heterostructures: a hybrid density functional theory study, Appl. Surf. Sci. 427 (2018) 487–498, https://doi.org/10.1016/j.apsusc.2017.09.019.

[43] Z. Zhou, Z. Shen, C. Song, M. Li, H. Li, S. Zhan, Boosting the activation of molecular oxygen and the degradation of tetracycline over high loading Ag single atomic catalyst, Water Res 201 (2021) 117314, https://doi.org/10.1016/j watres.2021.117314.

[44] Y. Zhao, X. Fan, H. Zheng, E. Liu, J. Fan, X. Wang, Bi_2WO_6/$AgInS_2$ S-scheme heterojunction: efficient photodegradation of organic pollutant and toxicity evaluation, J. Mater. Sci. Technol. 170 (2024) 200–211, https://doi.org/10.1016/j.jmst.2023.06.022.

Enhancement of photocatalytic activity of 2D/2D Sb_2WO_6/g-C_3N_4 Z-scheme heterojunction *via* effective interfacial charge transfer

Jinxin Liu[a], Jinyuan Liu[a,b*], Qichang Peng[a], Bin Wang[b*], Xingwang Zhu[c], Xue Gao[a], Huaming Li[a], Hui Xu[a, d*], Paul K. Chu[b*]

[a] School of the Environment and Safety Engineering, Institute for Energy Research, Jiangsu University, 301 Xuefu Road, Zhenjiang, 212013, P. R. China

[b] Department of Physics, Department of Materials Science and Engineering, and Department of Biomedical Engineering, City University of Hong Kong, Tat Chee Avenue, Kowloon, Hong Kong, China

[c] Institute of Technology for Carbon Neutralization, College of Environmental Science and Engineering, Yangzhou University, Yangzhou 225009, China

[d] Jiangsu Collaborative Innovation Center of Technology and Material of Water Treatment, Suzhou University of Science and Technology, Suzhou, 215009, P.R. China

***Corresponding authors:** *jyliu@ujs.edu.cn (J. Liu), bwang63@cityu.edu.hk (B. Wang), xh@ujs.edu.cn (H. Xu), paul.chu@cityu.edu.hk (P.K. Chu)*

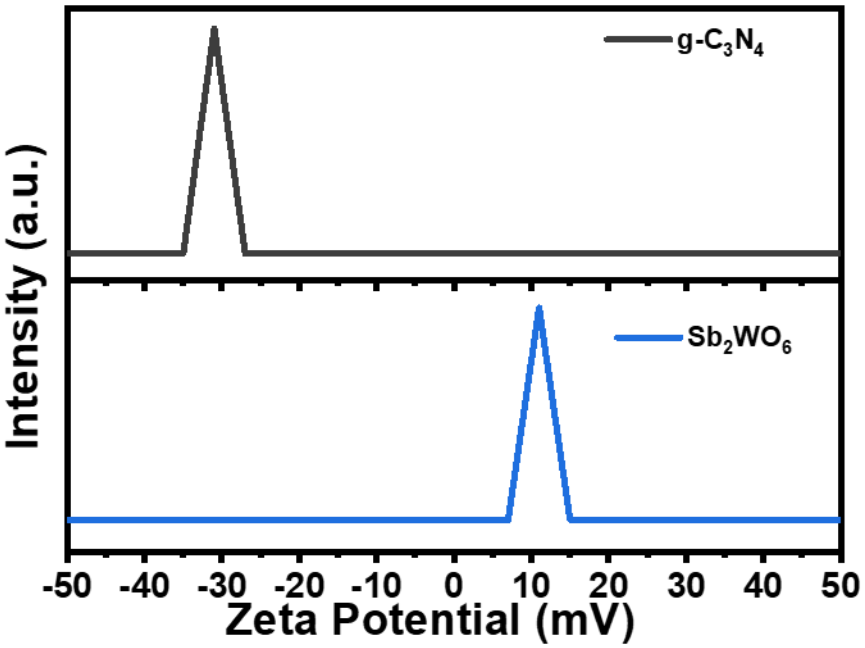

Figure S1. zeta potentials of g-C_3N_4 and Sb_2WO_6 samples.

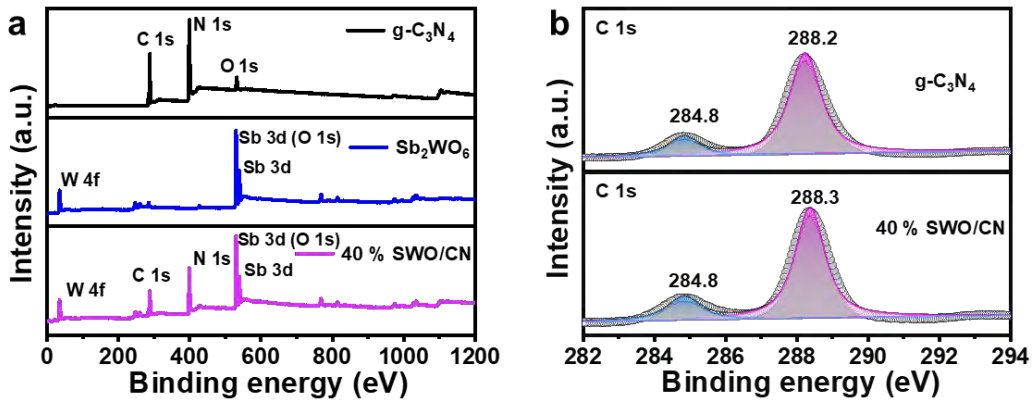

Figure S2. High-resolution XPS spectra of as-prepared samples: (a) survey, (b) C 1s

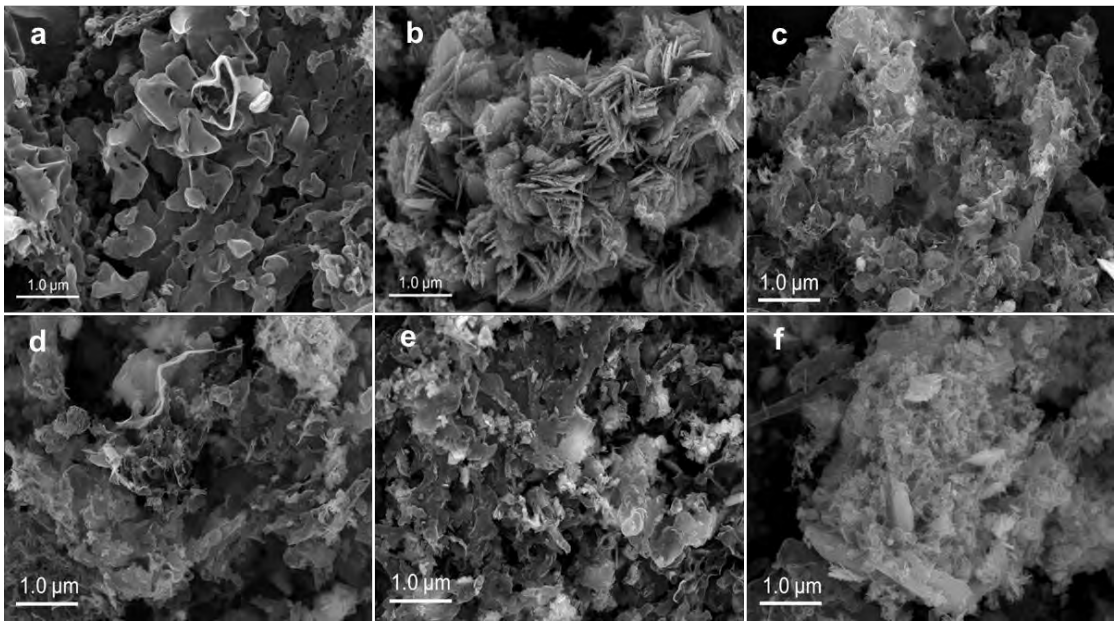

Figure S3. SEM images of (a) g-C3N4, (b) Sb2WO6, (c) 20% SWO/CN, (d) 30% SWO/CN, (e) 40% SWO/CN, (f) 50% SWO/CN.

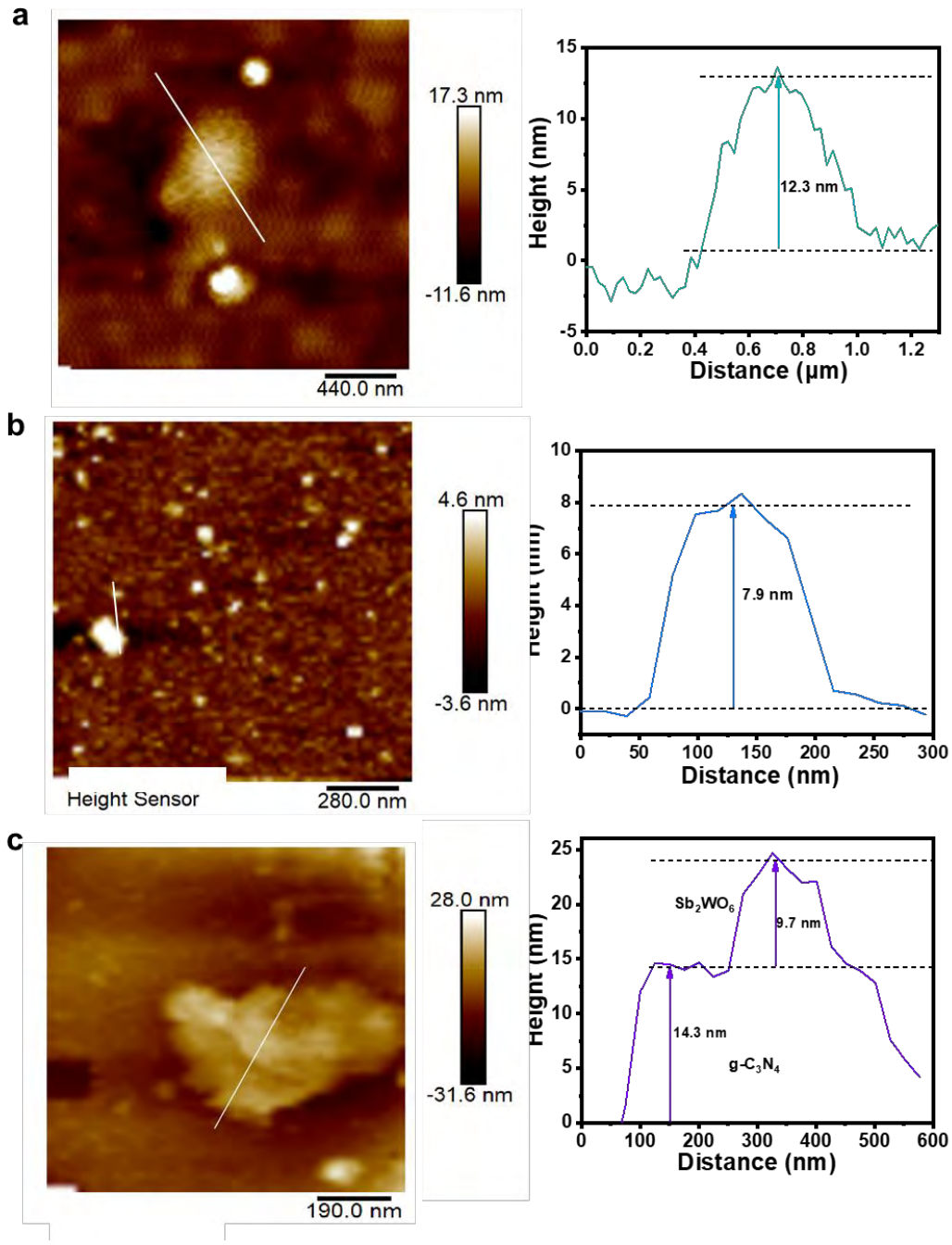

Figure S4. The AFM images of (a) g-C_3N_4; (b) Sb_2WO_6; (c) 40% SWO/CN

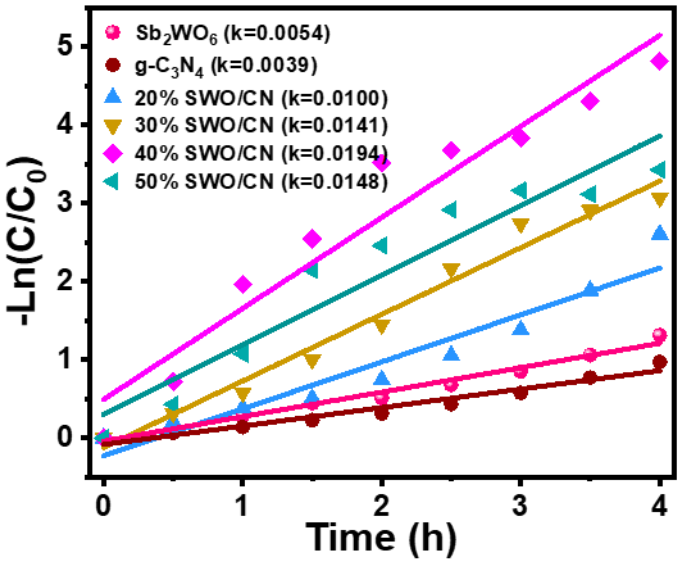

Figure S5. Quasi-first-order kinetic graph of photodegradation of RhB in the prepared sample.

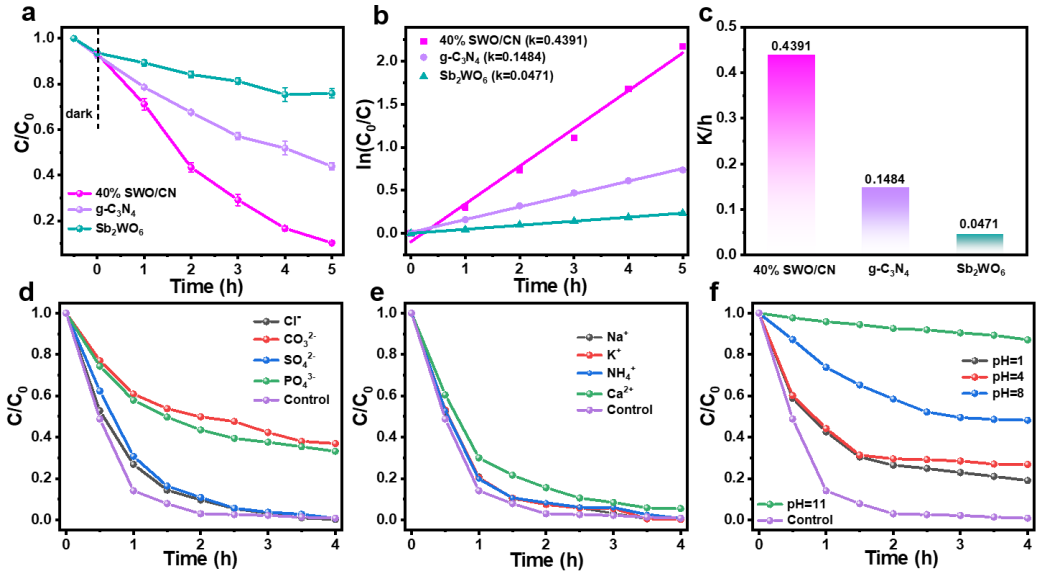

Figure S6. (a) Photocatalytic performance for degradation of MBT; (b) Simulated first-order reaction kinetics curve; (c) Pseudo-first-order rate constants; RhB degradation activity of 40% SWO/CN samples under different (d) anion, (e) cation and (f) PH conditions

Table S1. Comparison of degradation performance of different photocatalysts

Photocatalyst	Contaminant	Degradation efficiency	Light Source	Ref.
Sb_2WO_6/AgCl	RhB (50 mL, 20 mg/L)	82%,120 min	White light LED	[1]
S dots/MoS_2-PSS	RhB (50 mL, 4×10^{-5} g/mL)	88%,120 min	300 W (Xe lamp)	[2]
CQDs/Sb_2WO_6	RhB (100 mL,10 mg/L)	83%, 120 min	Xe lamp (300W)	[3]
Sn BiOCl/Bi_2WO_6	RhB (100 mL, 10 mg/L)	84.82%, 120 min	250 W (Xe lamp)	[4]
$SRP_{0.03}$/CdS HNS	RhB (100 mL, 10 mg/L)	88%, 120min	400 W (tungsten lamp)	[5]
OV-Sb_2WO_6-20	RhB (50 mL, 10 mg/L)	72%, 6 hour	250 W (Xe lamp)	[6]
MT-3	RhB (100 mL, 20 mg/L)	94.53%, 180min	300 W (Xe lamp)	[7]
Sb_2WO_6/g-C_3N_4	RhB (50 mL, 10 mg/L)	96%, 120min	250 W (Xe lamp)	This paper

Table S2. Elemental content analysis of synthetic samples.

\	N%	C%	Sb%	W%
20% SWO/CN	52.1	30.2	8.0	5.0
30% SWO/CN	46.3	26.9	10.1	8.0
40% SWO/CN	41.7	23.1	15.3	12.7
50% SWO/CN	34.3	21.0	20.2	16.3

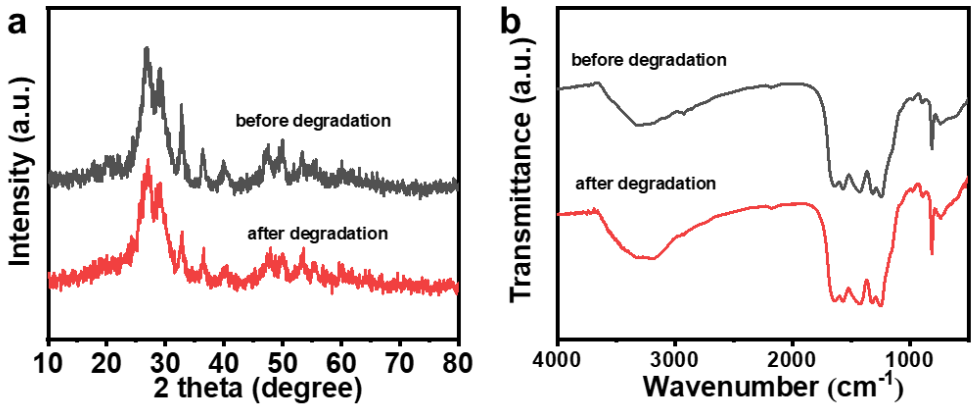

Figure S7. (a) XRD; (b) FT-IR patterns of 40% SWO/CN material before and after the recycle experiment.

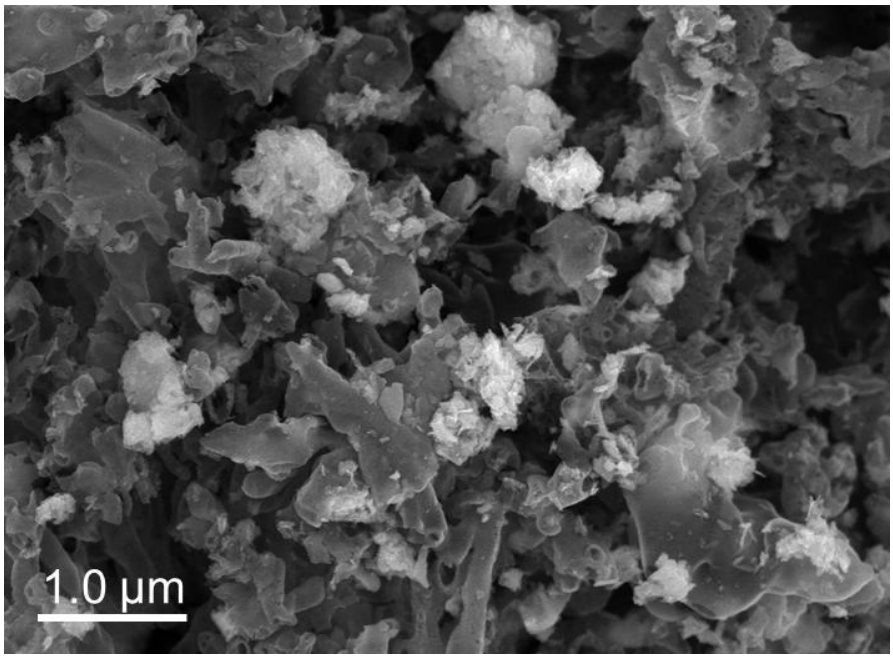

Figure S8. SEM patterns of 40% SWO/CN material before and after the recycle experiment

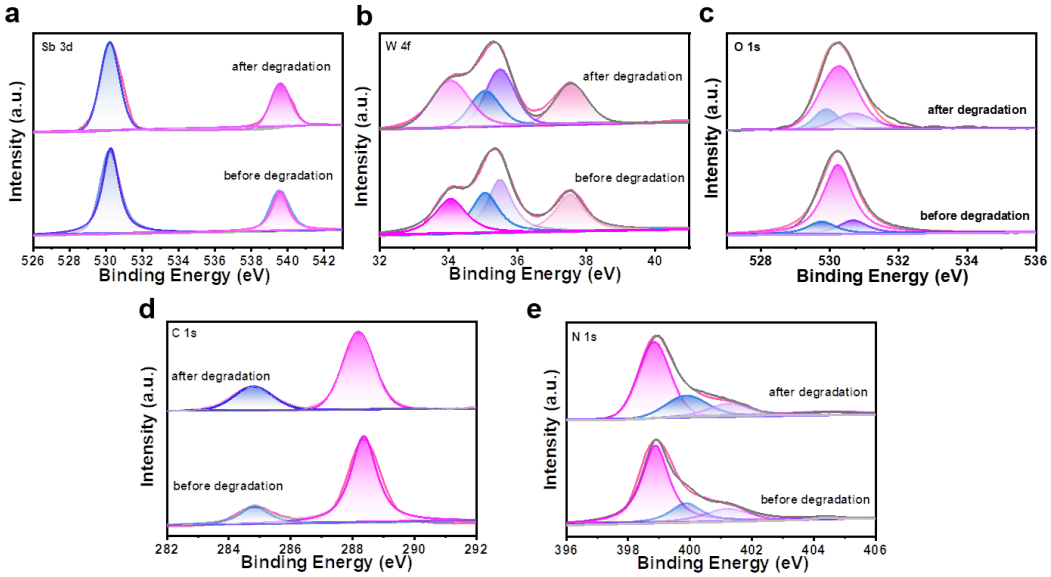

Figure S9. XPS patterns of 40% SWO/CN material before and after the recycle experiment.

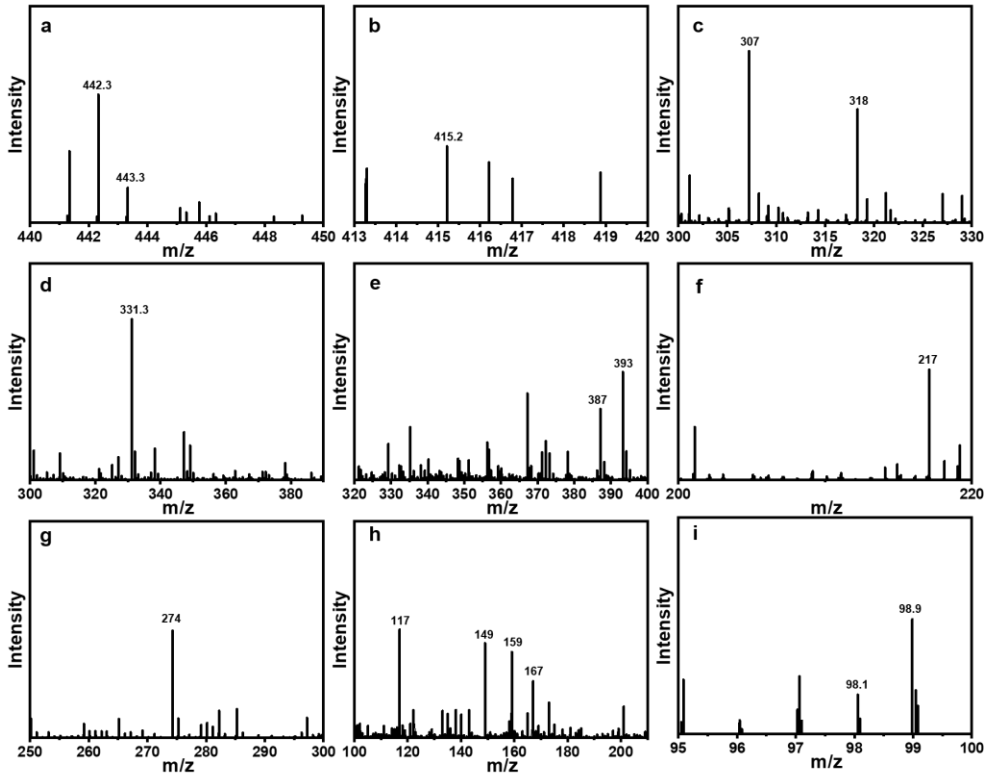

Figure S10. Mass spectra of RhB conversion products from 40% SWO/CN photodegradation under visible light.

References

[1] T. Zhang, L. Liu, Y. Luo, L. Sheng, H. Xua, R. Zhang, Y. Wang, Facile construction of Sb_2WO_6/AgCl heterojunction for enhanced photocatalytic degradation for rhodamineB and tetracycline, Inorg. Chem. Commun, 169 (2024) 113125, https://doi.org/10.1016/j.inoche.2024.113125.

[2] L. Shen, Y. Su, K. Zhao, C. Yu, J. Tang, Y. Li, N. Liu, Ligand-controlled photocatalysis of sulfur dots/MoS2 nanocomposite for degradation of dye and antibiotic, J. Alloys Compd, 984 (2024) 173975, https://doi.org/10.1016/j.jallcom.2024.173975.

[3] W. Li, Z. Wang, Y. Li, J. B. Ghasemi, J. Li, G. Zhang, Visible-NIR light-responsive 0D/2D CQDs/Sb_2WO_6 nanosheets with enhanced photocatalytic degradation performance of RhB: Unveiling the dual roles of CQDs and mechanism study, J. Hazard. Mater, 424 (2022) 127595, https://doi.org/10.1016/j.jhazmat.2021.127595.

[4] X. Xu, G. Liu, L. Li, N. Shan, B. Wang, M. Ji, J. Xia, H. Li, In-situ construction of Sn-doped BiOCl/Bi2WO6 heterojunction for excellent organic pollutants degradation: Insight into performance and mechanism, Appl. Surf. Sci., 635 (2023) 157512, https://doi.org/10.1016/j.apsusc.2023.157512.

[5] Ahmed Th. Abdulghaffar, Gomaa Khabiri b, Hemdan S.H. Mohamed, A no vel SRP/CdS heterostructure hollow nanospheres for outstanding photocatalytic performance, Sep. Purif. Technol., 326 (2023) 124813. https://doi.org/10.1016/j.seppur.2023.124813.

[6] Q. Peng, Q. Ruan, B. Wang, J. Liu, C. Huang, X. Zhu, D. Li, L. Liu, Y. Wang, X. Zhang, P. K. Chu, H. Xu, Low-temperature plasma-induced porous Sb2WO6

microspheres with rich oxygen vacancies to promote high-performance photocatalytic activity, Colloid Surface A, 681 (2024) 132724. https://doi.org/10.1016/j.colsurfa.2023.132724.

[7] J. Huang, Q. Li, J. He, J. Fu, L. Zhou, Q. Zhang, C. Yuan, Dye-sensitized n-n heterojunction {001}TiO2@NH2-MIL-101(Fe) for degradation of rhodamine B under visible light, Colloid Surface A, 707 (2025) 135886, https://doi.org/10.1016/j.colsurfa.2024.135886.